

Cascade dual-sites enable low-concentration NO-to-NH₃ electrosynthesis in neutral media

Tongwei Wu,^{3,‡} Xiaoxi Guo,^{1,‡} Hengfeng Li,² Yanning Zhang,³ Chao Ma,⁴ Hongmei Li,¹ Liyuan Chai,⁵ Haitao Zhao⁶ and Min Liu^{1,5*}

¹Hunan Joint International Research Center for Carbon Dioxide Resource Utilization, State Key Laboratory of Powder Metallurgy, School of Physics, Central South University, Changsha, 410083, China.

²School of Materials Science and Engineering, Central South University, Changsha, 410083, China.

³Institute of Fundamental and Frontier Sciences, University of Electronic Science and Technology of China, Chengdu 610054, Sichuan, China.

⁴College of Materials Science and Engineering, Hunan University, Changsha 410082, China.

⁵School of Metallurgy and Environment, Central South University, Changsha 410083, China

⁶Department of Electrical and Electronic Engineering, The Hong Kong Polytechnic University, Hong Kong, China

[‡]T. Wu and X. Guo contributed equally to this work.

*Correspondence and requests for materials should be addressed to M.L. (email: minliu@csu.edu.cn)

Abstract

Electrosynthesis of NH_3 from low-concentration NO (NORR) in neutral media offers a sustainable nitrogen fixation strategy but is hindered by weak NO adsorption, slow water dissociation, and sluggish hydrogenation kinetics. Herein, we propose a new strategy that successfully overcomes these limitations through using an electron-donating motif to modulate NO-affinitive catalysts, thereby creating dual active site with synergistic functionality. Specifically, we integrate electron-donating nanoparticles into a Fe single-atom catalyst (Fe_{SAC}), where Fe sites ensure strong NO adsorption, while electron-donating motifs promote water dissociation and NO hydrogenation. *In situ* X-ray absorption spectroscopy (XAS), *in situ* attenuated total reflection-infrared spectroscopy (ATR-IR), and theoretical calculations reveal that electron-donating motifs increase Fe site electron density, strengthening NO adsorption. Additionally, these motifs also promote water dissociation, supplying protons to lower the NO hydrogenation barrier. This synergistic interplay enables a cascade reaction mechanism, delivering a remarkable Faradaic efficiency (FE) of 90.3% and a NH_3 yield rate of $709.7 \mu\text{g h}^{-1} \text{mg}_{\text{cat}}^{-1}$ under 1.0 vol% NO in neutral media, outperforming pure Fe_{SAC} (NH_3 yield rate: $444.2 \mu\text{g h}^{-1} \text{mg}_{\text{cat}}^{-1}$, FE: 56.6%) and prior high-NO-concentration systems. Notably, a record NH_3 yield of $3123.8 \mu\text{g h}^{-1} \text{mg}_{\text{cat}}^{-1}$ was achieved in a membrane electrode assembly (MEA) electrolyzer under a 1.0 vol% NO. This work establishes a new paradigm in NORR by simultaneously enhancing NO adsorption, water dissociation, and hydrogenation kinetics, providing a scalable route for efficient NH_3 electrosynthesis from dilute NO sources.

Introduction

Nitric oxide (NO) is a harmful atmospheric pollutant primarily emitted from industrial processes and vehicle exhaust, posing severe environmental and health risks.¹⁻¹⁰ Electrochemical NO reduction (NORR) under mild conditions, utilizing renewable electricity and water, offers a sustainable route to both NO removal and ammonia (NH₃) production—an essential fertilizer and potential hydrogen carrier—via a carbon-free process.¹¹⁻¹³ Large-scale NORR requires neutral water conditions to enable earth-abundant transition metal catalysts, which are unstable in acidic media, and to facilitate direct seawater use without desalination.^{14,15} However, its efficiency in neutral media is severely restricted by low NO solubility, sluggish water dissociation, and slow NO hydrogenation kinetics.

Most current research focuses on engineering electron-deficient sites to strengthen NO adsorption for NORR under neutral media, even at low NO concentrations.¹⁶⁻²³ Among these catalysts, Fe-based catalysts exhibit remarkable efficiency in enhancing the performance of low-concentration NORR.^{19,22,23} This becomes particularly effective when Fe sites are in a low oxidation state with sharp d-state defect features, enabling energy-aligned orbital configurations that facilitate the adsorption and activation of NO molecules.¹⁹ Moreover, as one of the most cost-effective and abundant elements in the earth,²⁴ Fe also plays a pivotal role in biological nitrogenases, enabling efficient natural nitrogen fixation.²⁵ However, the current approach of enhancing NO affinity on catalysts overlooks the critical challenge of inherently slow water dissociation and NO hydrogenation kinetics in neutral media.

Electron-donating materials have demonstrated significant catalytic efficiency in water dissociation reactions,²⁶ which are essential for supplying protons to promote NO hydrogenation.¹⁸⁻²¹ Inspired by aforementioned guidance, we propose a novel and universal strategy to improve neutral NORR performance by integrating electron-donating motifs into NO-affinitive catalysts, forming a dual-active-site architecture with synergistic functionality. To demonstrate this strategy and its underlying mechanism, we selected Pt nanoparticles (Pt_{NPs}) as the electron donor, incorporated into an Fe single-atom catalyst (Fe_{SAC}) with NO-affinitive ability, as a representative case for detailed analysis. *In situ* X-ray absorption spectroscopy (XAS), attenuated total reflection-infrared spectroscopy (ATR-IR), and density functional theory (DFT) calculations confirmed that Pt_{NPs} serve as electron donors, increasing the electron density at the Fe sites for stronger NO adsorption, while also facilitating water dissociation to supply protons and significantly promoting the subsequent hydrogenation of NO intermediate.

The synergistic interplay between these dual sites enables a cascade reaction mechanism. As a result, the Pt_{NPs}/Fe_{SAC} catalyst achieved a NH₃ yield rate of 709.7 $\mu\text{g h}^{-1} \text{mg}_{\text{cat.}}^{-1}$ and a Faraday efficiency (FE) of 90.3% at -0.6 V under 1.0 vol% NO/Ar in neutral media, outperforming Fe_{SAC} alone (NH₃ yield rate: 444.2 $\mu\text{g h}^{-1} \text{mg}_{\text{cat.}}^{-1}$, FE: 56.6%) and surpassing previously reported NORR systems under high NO concentrations (above 10%) in various medias. Notably, in a membrane electrode assembly (MEA) electrolyzer, the system achieved a record-breaking NH₃ yield of 3123.8 $\mu\text{g h}^{-1} \text{mg}_{\text{cat.}}^{-1}$. This approach was successfully extended to other

electron-donating nanoparticles, such as Au, highlighting its broad applicability for efficient NORR in neutral media.

Results

Computational predictions

DFT calculations were performed to understand the mechanism underlying the enhanced NORR activity. Fe single atoms coordinated with pyridine-4N in graphene (FeN₄) were chosen as the catalyst model due to their high stability (Fig. 1a).²⁷ To simulate the nanoparticle environment, nine Pt atoms were introduced into the FeN₄ structure (FeN₄-Pt, Fig. 1b). Before Pt loading, Fe single atom in FeN₄ exhibited partially unoccupied orbitals above the Fermi level (Fig. 1c). After Pt loading, these unoccupied orbitals shifted towards the Fermi level, indicating electron injection into Fe (Fig. 1d). Bader charge analysis confirmed that Fe received $\sim 0.12e^-$ (Fig. 1e), increasing its electron density and reactivity.²⁸

We firstly investigated water dissociation on both FeN₄ and FeN₄-Pt sites (Fig. 1f and 1g). On FeN₄ site, the dissociation of H₂O into *H and *OH required a free energy of 1.45 eV. However, in FeN₄-Pt, H₂O adsorbed at Pt sites, reducing the dissociation energy to 0.99 eV, demonstrating the role of Pt in facilitating proton supply for NORR.

Next, the free energy pathway for NO to NH₃ conversion was calculated and a significant enhancement in the NO adsorption capability on FeN₄-Pt (-1.36 eV) compared to FeN₄ (0.05 eV) was revealed (Fig. 1h). The first proton step (*NO → *HNO) was energetically favorable on both catalysts, but the activation barrier was

reduced from 1.50 eV (FeN_4) to 0.54 eV ($\text{FeN}_4\text{-Pt}$). The second protonation led to the formation of $^*\text{NH}_2\text{O}$ ($\text{FeN}_4\text{-Pt}$, $\Delta G = 0.55$ eV) instead of $^*\text{HNOH}$ (FeN_4 , $\Delta G = 0.40$ eV), thus shifting the reaction pathway. The third protonation on $\text{FeN}_4\text{-Pt}$ led to $^*\text{NH}_2\text{OH}$ formation, but its high desorption energy (3.18 eV) made $^*\text{NH}_2\text{OH}$ an unlikely byproduct. Instead, $^*\text{NH}_2\text{OH}$ underwent hydrogenation to $^*\text{NH}_2 + \text{H}_2\text{O}$, followed by an exothermic step to NH_3 ($\Delta G = 0.23$ eV).

Overall, Pt_{NPs} enhance NORR by donating electrons to Fe, strengthening NO adsorption, and accelerating water dissociation to supply protons for NO hydrogenation. This synergistic cascade mechanism significantly boosts NH_3 synthesis efficiency in neutral low-concentration NO conditions (Fig. 1i).

Catalyst characterization

The Fe_{SAC} and $\text{Pt}_{\text{NPs}}/\text{Fe}_{\text{SAC}}$ catalysts were synthesized based on computational guidance. Fe_{SAC} was synthesized through pyrolysis followed by acid etching, while Pt_{NPs} were subsequently loaded onto Fe_{SAC} by a thermal reduction method. High-aberration-corrected high-angle annular dark-field scanning transmission electron microscopy (HAADF-STEM) image of Fe_{SAC} (Fig. 2a) revealed that isolated atomic sites are randomly dispersed on nitrogen doped carbon (NC) without observable metal clusters or particles, consistent with the X-ray diffraction (XRD, Supplementary Fig.1) result. Inductively coupled plasma optical emission spectrometer (ICP-OES) confirmed a Fe content of 0.66 wt% in Fe_{SAC} (Table S1).

In contrast, HAADF-STEM images of $\text{Pt}_{\text{NPs}}/\text{Fe}_{\text{SAC}}$ showed Pt_{NPs} with a size of ~ 3 nm and a lattice distance of 0.214 nm, corresponding to the (111) crystal plane (Fig.

2b). XRD pattern further confirmed the presence of Pt_{NPs} (Supplementary Fig.1). As illustrated in Fig. 2c, Fe_{SAC} are densely distributed around Pt nanoparticles, and energy dispersion X-ray spectroscopy (EDX, Fig. 2d) mapping confirmed the uniform dispersion of Fe, C, and N elements, with Pt as the primary nanoparticle component. ICP-OES results showed Fe and Pt contents of 0.62 wt% and 0.84 wt%, respectively (Table S1).

To investigate the chemical state and atomic structure, X-ray absorption spectroscopy (XAS) and X-ray photoelectron spectroscopy (XPS) were employed. The Fe K-edge X-ray absorption near-edge structure (XANES) spectra revealed that Fe in Fe_{SAC} lies between +2 and +3 oxidation states (Fig. 2e). Notably, Pt incorporation induces a negative shift in the Fe K-edge, indicating a reduced Fe oxidation state.

Fourier transformed (FT) k^2 -weighted extended X-ray absorption fine structure (EXAFS) analysis (Fig. 2f) confirmed the absence of Fe clusters, as FePc, Fe_{SAC} and Pt_{NPs}/Fe_{SAC} exhibited a prominent Fe-N scattering peak at 1.51 Å.^{29,30} EXAFS fitting curves revealed that the average coordination numbers of Fe_{SAC} and Pt_{NPs}/Fe_{SAC} are 4.4 and 4.2, respectively, indicating that Fe is coordinated with four nitrogen atoms (Fe-N₄) in both systems. The bond lengths for Fe-N are 1.96 and 1.97 Å, respectively (Supplementary Fig.2 and Table S2). Additionally, wavelet transform (WT) analysis of Fe K-edge EXAFS oscillations (Supplementary Fig.3) displays a strong signal with a maximum intensity at 3.8 Å⁻¹ for Pt_{NPs}/Fe_{SAC}, corresponding to the Fe-N first coordination shell, which is similar to Fe_{SAC}.²⁹ Impressively, no Fe-Fe signal was

detected in WT contour plots for either Fe_{SAC} or Pt_{NPs}/Fe_{SAC}, further confirming the atomically dispersed Fe in both catalysts.

XPS analysis of the Pt 4f region (Fig. 2g) showed two Pt⁰ peaks at 71.8 (4f_{7/2}) and 75.1 eV (4f_{5/2}) along with two Pt²⁺ peaks at 72.7 (4f_{7/2}) and 76.0 eV (4f_{5/2}) in Pt_{NPs}/Fe_{SAC} (Fig. 2g), likely due to partial surface oxidation or electron donation from adjacent Fe atoms.^{31,32} The successful synthesis and characterization of Pt_{NPs}/Fe_{SAC} confirmed its distinct structural features, including reduced Fe oxidation states upon Pt incorporation and stable Fe-N₄ coordination.

Effect of Pt_{NPs}/Fe_{SAC} in low concentration NORR

To investigate the dynamic catalytic process of NORR, *in situ* electrochemical XAS and attenuated total reflection-infrared (ATR-IR) spectroscopies were conducted. As shown in Fe K-edge XANES spectra of Pt_{NPs}/Fe_{SAC} (Fig. 3a), the white-line peak intensity increased as the applied potential decreases from open circuit potential (OCP) to -0.3 V, indicating that NO adsorption on Fe sites leads to an increase in coordination number. A shift of the adsorption edge to higher energy suggested an increased oxidation state of Fe. As the potential further decreased to -0.6 V, the white-line peak intensity diminished, implying NO consumption and reduction of Fe valence state, confirming Fe_{SAC} as the real active sites.

The EXAFS spectra (Fig. 3b) further revealed the dynamic evolution of Fe's local coordination. The Fe-N peak was enhanced with decreasing the applied potentials, suggesting that the intermediates adsorb on Fe sites. A notable negative shift from OCP to -0.3 V, suggested the formation of a shorter Fe-N bond due to NO adsorption.

When the potential was further reduced to -0.6 V, the peak moved from 1.53 to 1.58 Å, signaling the occurrence of NORR and aligning well with the XANES results.

Next, *in situ* ATR-IR spectroscopy was employed to identify the adsorbed intermediates. As shown in Fig. 3c and 3e, both Fe_{SAC} and Pt_{NPs}/Fe_{SAC} displayed peaks corresponding to NO adsorption, including vertical mode (1774 cm⁻¹, NO_v) and bent mode (1695 cm⁻¹, NO_b).^{19,33} The higher intensity of these peaks in Pt_{NPs}/Fe_{SAC} indicated stronger NO adsorption. With the potentials shifted from OCP to -1.0 V, the intensity of NO_b peak increased, suggesting effective NO activation at Fe sites. As illustrated in Fig. 3d and 3f, the NO_b peak intensity in Pt_{NPs}/Fe_{SAC} spectra is much stronger than that of Fe_{SAC}, implying that the lower valence state of Fe site induced by introduction of Pt nanoparticles is more conducive to activate NO, in agreement with the DFT results.

Compared to Fe_{SAC}, the peak of -OH bending vibration at 1648 cm⁻¹ was strengthened in Pt_{NPs}/Fe_{SAC} spectra, indicating that the Pt nanoparticles facilitate H₂O electrolysis to produce *H, which is beneficial for subsequent NO hydrogenation (Fig. 3d and 3f).^{34,35} This was further verified by the electron paramagnetic resonance (EPR) technique using 5,5-dimethyl-1-pyrroline-N-oxide (DMPO) as a hydrogen radical (·H) trapping reagent.^{36,37} As shown in Supplementary Fig.5, distinct ·H signals were detected for Pt_{NPs}/Fe_{SAC} but absent in Fe_{SAC}, confirming enhanced hydrogen generation. Hydrogenated intermediates NH_x (1412 and 1530 cm⁻¹) were progressively formed at lower potentials, ultimately converting to NH₄⁺ (1465 cm⁻¹).³⁸⁻⁴⁰ Overall, these results clearly demonstrated Pt_{NPs} served as electron donors,

increasing Fe site electron density to enhance NO adsorption while simultaneously promoting water dissociation to supply protons for efficient NORR.

NORR performance evaluation

The NORR performance was evaluated in 0.5 M K₂SO₄ electrolyte, using an air-tight H cell. Prior to electrolysis, high-purity Ar was purged into the electrolyte to remove residual oxygen. As shown in Fig. 4a, the linear sweep voltammetry (LSV) curves revealed a significant increase in current density for Pt_{NPs}/Fe_{SAC} in 1 vol% NO atmosphere compared to Ar-saturated conditions, confirming effective NO reduction on the catalyst surface. Compare to Fe_{SAC}, Pt_{NPs}/NC and NC, the Pt_{NPs}/Fe_{SAC} showed the largest current density gap, indicating superior NORR activity (Supplementary Fig.6).

As depicted in Fig. 4b, the NH₃ yield rate and FE of Pt_{NPs}/Fe_{SAC} increase steadily with applied potentials from -0.4 to -0.6 V, reaching the maximum values of 709.7 μg h⁻¹ mg_{cat.}⁻¹ and 90.3% at -0.6 V, outperforming previously reported NORR catalysts (Table S4). NH₃ quantification via colorimetric method (Supplementary Fig.7) and nuclear magnetic resonance (NMR) spectroscopy (Supplementary Fig.8) yielded consistent results, ensuring measurement accuracy (Supplementary Fig.14). However, at the applied potentials beyond -0.6 V, NORR performance of Pt_{NPs}/Fe_{SAC} declined due to the competing HER. In comparison, Fe_{SAC} obtained its highest NORR performance at -0.7 V with a NH₃ yield of 444.2 μg h⁻¹ mg_{cat.}⁻¹ and FE of 56.6% (Fig. 4c and S9), while Pt_{NPs}/NC and bare NC exhibited negligible NORR activity (Fig. 4c).

DFT and *in-situ* electrochemical experiments clearly verified that Pt_{NPs} served as

electron donors, increasing the electron density at the Fe single-atom site to promote NO adsorption, while facilitating water dissociation for proton supply. This dual role enabled efficient NO-to-NH₃ conversion with high activity and selectivity.

To validate that NH₃ originated from NO reduction, control experiments were conducted under three conditions: (1) electrolysis at -0.6 V in Ar-saturated electrolyte, (2) testing at OCP in NO-saturated electrolyte, and (3) testing in NO-saturated electrolyte with bare carbon paper (CP) as work electrode (Fig. 4d). Only negligible NH₃ was detected in these cases, confirming that NH₃ formation on Pt_{NPs}/Fe_{SAC} exclusively results from NO reduction. Additionally, an isotope labeling experiment was performed to exclude the possibility of nitrogen contamination. The laboratory-produced ¹⁵N₂O was used as the feeding gas for NORR at -0.6 V for 1 h. As shown in Fig. 4e, the NMR analysis conclusively verified that the generated NH₃ is originated from NO.

Electrocatalyst stability is crucial for long-term energy conversion and storage. Pt_{NPs}/Fe_{SAC} demonstrated excellent durability, maintaining stable NH₃ yield and FE over ten consecutive cycles (Fig. 4f). A long-term stability test (>70 h, Supplementary Fig.15) showed no significant decline in current density, further confirming its robust electrochemical stability. Post-reaction characterization revealed minor catalyst changes: XRD pattern showed weakened Pt diffraction peaks, suggesting partial Pt dissolution (Supplementary Fig.16). ICP analysis detected trace amounts of Pt in the electrolyte post-NORR (Table S3). XANES analysis exhibited a slight increase in Fe valence state after NORR test (Supplementary Fig.17a). EXAFS spectra revealed no

Fe-Fe bond formation, confirming Fe remains atomically dispersed (Supplementary Fig.17b).

To mitigate NO mass transport limitations due to its low solubility ($\sim 1.92 \text{ mmol L}^{-1} \text{ atm}^{-1}$ in water at 25°C), NORR was conducted in a membrane electrode assembly (MEA) electrolyzer.^{41,42} Compared to H-cell, the MEA significantly enhanced current density, suggesting improved NO utilization (Fig. 4g). As shown in Fig. 4h, increasing the applied cell voltage from 1.2 to 1.6 V leads to higher NH_3 yield and FE. Notably, $\text{Pt}_{\text{NPs}}/\text{Fe}_{\text{SAC}}$ achieved a record-breaking NH_3 yield of $3123.8 \mu\text{g h}^{-1} \text{ mg}_{\text{cat}}^{-1}$ and FE of 94.5% at 1.6 V (Fig. 4h), surpassing all previously reported NORR catalyst even tests under high NO concentration (Fig. 4i).

To explore alternative metal nanoparticles, $\text{Au}_{\text{NPs}}/\text{Fe}_{\text{SAC}}$ was synthesized for NO-to- NH_3 conversion. TEM images (Supplementary Fig.18) and XRD patterns (Supplementary Fig.19) clearly verified that successful Au nanoparticle deposition. The obtained $\text{Au}_{\text{NPs}}/\text{Fe}_{\text{SAC}}$ achieved optimal NH_3 yield of $595.4 \mu\text{g h}^{-1} \text{ mg}_{\text{cat}}^{-1}$ and FE of 78.9% at -0.5 V, further demonstrating the versatility of metal-modified Fe_{SAC} systems.

Conclusions

In summary, we present an electron-donating particle-mediated strategy that integrates Pt_{NPs} as the electron donor into the Fe_{SAC} electrocatalyst to construct dual-active-site architectures, thereby enhancing NO adsorption while promoting water dissociation and NO hydrogenation for significantly improving neutral NORR at low NO concentration (1 vol%). *In situ* spectro-electrochemical experiments,

coupled with theoretical calculations, confirmed that the Pt nanoparticles serve as electron donors, increasing the electron density at the Fe single-atom site to promote NO adsorption, while facilitating water dissociation to provide protons and thus reducing the activation energy of NO hydrogenation. The synergistic interplay between these dual sites enables a cascade reaction mechanism achieving a superior NORR performance with a NH_3 FE up to 90.3% and a high NH_3 yield rate of $709.7 \mu\text{g cm}^{-2} \text{ h}^{-1}$ under 1 vol% NO concentration at -0.6 V, outperforming Fe_{SAC} (NH_3 yield rate: $444.2 \mu\text{g h}^{-1} \text{ mg}_{\text{cat.}}^{-1}$, FE: 56.6%) and prior high-NO-concentration systems. Notably, in a MEA electrolyzer, the system achieved a record-breaking NH_3 yield of $3123.8 \mu\text{g h}^{-1} \text{ mg}_{\text{cat.}}^{-1}$. This work not only offers an attractive earth-abundant nanocatalyst for NH_3 electrosynthesis at low NO concentrations, but also provides a novel methodology for designing superior electrocatalytic NORR systems through a dual-active-site strategy, paving the way for large scale NH_3 electrosynthesis.

Methods

Chemicals

Ketjen black ecp600JD (KJ), Nafion and carbon paper (CP) were purchased from Suzhou Sinero Technology Co., Ltd (Suzhou, China). Sodium hydroxide (NaOH), sodium nitrite (NaNO_2), p-aminobenzenesulfonic acid (pAA, $\text{C}_6\text{H}_7\text{NO}_3\text{S}$) m-phenylenediamine (mPDA, $\text{C}_6\text{H}_8\text{N}_2$) ammonium persulfate ($(\text{NH}_4)_2\text{S}_2\text{O}_8$), iron chloride hexahydrate ($\text{FeCl}_3 \cdot 6\text{H}_2\text{O}$), polyvinylpyrrolidone (PVP), sodium hypochlorite (NaClO) and ethylene glycol (EG) were obtained from Aldrich Chemical

Reagent Co., Ltd. (Shanghai, China). Chloroplatinic acid hexahydrate ($\text{H}_2\text{PtCl}_6 \cdot 6\text{H}_2\text{O}$), gold chloride trihydrate ($\text{HAuCl}_4 \cdot 3\text{H}_2\text{O}$), salicylic acid ($\text{C}_7\text{H}_6\text{O}_3$), trisodium citrate dihydrate ($\text{Na}_3\text{C}_6\text{H}_5\text{O}_7 \cdot 2\text{H}_2\text{O}$), sodium nitroferricyanide (III) dihydrate ($\text{Na}_2\text{Fe}(\text{CN})_5\text{NO} \cdot 2\text{H}_2\text{O}$), dimethyl sulfoxide ($\text{DMSO-}d_6$), ammonium chloride ($^{14}\text{NH}_4\text{Cl}$, $^{15}\text{NH}_4\text{Cl}$), sodium borohydride (NaNH_4), sodium nitrite ($\text{Na}^{15}\text{NO}_2$) were bought from Macklin Chemical Reagent Co., Ltd. (Shanghai, China). Fe powder, potassium thiocyanate (KSCN) and hydrochloric acid (HCl) were supplied by Sinopharm Chemical Reagent Co., Ltd. (Shanghai, China). All the reagents were used as received. The water used throughout all experiments was purchased from Wahaha Group Co., Ltd. (Hangzhou, China).

Preparation of NC

1.0 g of KJ was dispersed in 30 mL H_2O and sonicated in an ice bath for 2 h to labeled A1. Separately, 0.74 g pAA was dissolved in 30 mL H_2O . To this solution, 9 mL of 1 M NaOH, 4 mL of 1 M NaNO_2 and 21 mL of 1 M HCl were added to prepare the diazo salt (labeled A2), maintain the reaction at 0°C . Subsequently, the A2 was mixed with A1. To initiate surface grafting of the diazonium salt, 0.7 g of reduced Fe powder was introduced. Afterward, 25 mL concentrated HCl , 7.6 g of mPDA, 23 mL of 1 M FeCl_3 and 70 mL of 2 M $(\text{NH}_4)_2\text{S}_2\text{O}_8$ solution were added, and the reaction was allowed to react overnight. After filtration, the product was washed with water for 3 times and vacuum drying overnight to yield the NC precursor.

Preparation of Fe_{SAC}

0.6 g of the NC precursor was ultrasonically dispersed in 30 mL H_2O , followed by the

addition of 1.8 mL of 1 M FeCl_3 and 6 mL of 1 M KSCN. The solvent was removed by rotary evaporation, and the residue was heated to 950 °C for 1 h under an Ar atmosphere. The obtained black powder was dispersed in 50 mL of 1 M HCl solution overnight at 80 °C. Then, the powder was washed with water 3 times, and drying overnight. Finally, the dried powder was heated at 950 °C for 3 h in an Ar atmosphere to yield Fe_{SAC} .

Preparation of $\text{Pt}_{\text{NPs}}/\text{Fe}_{\text{SAC}}$

100 mg Fe_{SAC} was dispersed in 20 mL of EG. Next, 5 mg $\text{H}_2\text{PtCl}_6 \cdot 6\text{H}_2\text{O}$ was dispersed in 20 mL of EG and then dripped into Fe_{SAC} . The obtained suspension was stirred for 2 h at room temperature and then treated at 160 °C for 90 min. Afterward, the final product was washed 3 times and dried overnight. The Pt_{NPs} was synthesized by replacing the Fe_{SAC} to NC.

Preparation of $\text{Au}_{\text{NPs}}/\text{Fe}_{\text{SAC}}$

100 mg of Fe_{SAC} and 10 mg of PVP were dispersed in 30 mL H_2O . Then, 400 μL of a 10 mg/mL HAuCl_4 solution was added dropwise, followed by 100 mg of NaNH_4 dissolved in 20 mL H_2O to reduce HAuCl_4 . The mixture was stirred for 10 min at room temperature.

Electrochemical measurements

Electrochemical measurements were performed with a CHI660E electrochemical station (CH Instruments, Inc., Shanghai) in a H-cell under ambient condition, which was separated by Nafion 211 membrane. The $\text{Pt}_{\text{NPs}}/\text{Fe}_{\text{SAC}}$, Ag/AgCl and graphite rod acted as the working electrode, reference electrode and counter electrode, respectively.

The reference electrode was calibrated to the reversible hydrogen electrode (RHE) scale in all measurements using the following equation: $E(\text{RHE}) = E(\text{Ag/AgCl}) + (0.059 \text{ pH} + 0.197) \text{ V}$. High purity Ar gas (99.999%) was bubbled into cathode chamber with the flow rate of 30 sccm for 30 min to removal oxygen before NORR. Then, the low-concentration NO (1% v/v) was firstly washed by 4 M KOH and then fed at 30 sccm for 30 min to saturate the electrolyte, maintain a constant flow during the electrochemical tests. For NORR tested in MEA, the RuO₂ supported on nickel foam (RuO₂/NF) as anode tested in 1 M KOH, while Pt_{NPs}/FeSAC was used as the cathode for NORR and the tail gas was absorbed by 1 M HCl.

Determination of NH₃

The produced NH₃ was quantified by the indophenol blue method⁴³ and NMR. For indophenol blue method, standard NH₃ solution with a series of concentrations were used to calibrated the concentration-absorbance curves. The fitting curve ($y = 0.3435x + 0.05843$, $R^2 = 0.9999$) showed good linear relation of absorbance value with NH₃ concentration. All electrolytes were diluted 10 times before testing unless otherwise specified. For ¹H NMR measurements, the electrolyte after electrolysis was diluted 2 times with 1 M HCl to adjust the pH to acidic. Then, 100 mL DMSO-d₆ was added in 500 μL acidified electrolyte.

Determination of FE and NH₃ Yield

The FE for NH₃ synthesis was calculated as the amount of electric charge used for NH₃ production divided by the total charge passed through the electrodes during electrolysis. The total amount of NH₃ produced was measured using colorimetric

methods. The FE could be calculated as follows:

$$FE = 3 \times F \times [NH_3] \times V / (17 \times Q) \times 100\% \quad (1)$$

NH₃ yield was calculated using the following equation:

$$NH_3 \text{ yield} = [NH_3] \times V / (m_{\text{cat.}} \times t) \quad (2)$$

where F is the Faraday constant, [NH₃] is the measured NH₃ concentration, V is the volume of the electrolyte in the cathodic chamber, Q is the total quantity of applied electricity; t is the reduction time; m_{cat.} is the loaded mass of catalyst on carbon paper.

Electrochemical *in situ* ATR-IR measurements

The *in situ* electrochemical ATR-IR measurements were conducted on a Nicolet iS50 FT-IR spectrometer with a liquid nitrogen-cooled MCT-A detector. The Si prism loaded with catalyst, Pt plate and Ag/AgCl were used as the working electrode, counter electrode and reference electrode, respectively, with 0.5 M K₂SO₄ as electrolyte. During the process of tests, 1% NO was bubbled into the electrolyte with the flow rate of 10 sccm. Prior to testing, the Si prism was coated with Au film. The Si prism was first polished by 100 nm Al₂O₃. Next, the Si prism was soaked in a piranha solution for 30 min to removal organic contaminants. Then, the reflecting surface was immersed in a mixture of the Au plating solution (5.75 mM NaAuCl₄·2H₂O + 0.025 M NH₄Cl + 0.075 M Na₂SO₃ + 0.025 M Na₂S₂O₃ + 0.026 M NaOH) and a 2 wt % HF solution at 60 °C for 5 min. Afterward, the Au film was rinsed with deionized water and dried with N₂. *In situ* ATR-IR spectra were collected at OCP and different applied potentials.

Electrochemical *in situ* XAFS measurements

The *in situ* XAFS measurements were conducted in the fluorescence mode using a home-made electrochemical cell. The Pt_{NPs}/FeSAC, Ag/AgCl and graphite rod were used as working electrode, reference electrode and counter electrode, respectively.

Relevant measurements were conducted in NO-saturated 0.5 M K₂SO₄ electrolyte. The XAS spectra were recorded at OCP and different applied potentials.

Computation and model details

All simulations were carried out using density functional theory as implemented in the GPAW software^{44,45} version 19.8.1. The exchange-correlation effects were accounted for using the BEEF-vdW-functional, which combines the generalized gradient approximation with the Langreth-Lundqvist van der Waals-functional to achieve accurate adsorption energies. A $2 \times 2 \times 1$ k-point mesh was used and all the calculations were spin-polarized. To model the solvent at the electrochemical interface, a hybrid implicit/explicit approach was employed, where 40 explicit water molecules surrounded the electrode surface, and the remaining water was modeled using the SCMVD⁴⁶ dielectric continuum model. The positions and orientations of the explicit water molecules were optimized using the minima hopping global optimization method⁴⁷ as implemented in ASE.⁴⁸

The free energies of the reaction intermediates were defined as by $\Delta G = \Delta E + \Delta ZPE - T\Delta S$, where ΔE , ΔZPE , T , and ΔS represent the reaction energy, zero-point energy, temperature (298.15 K), and the entropy, respectively.

Enhanced Sampling

The slow growth sampling approach^{49,50} in the constrained molecular dynamics simulation method can be used to describe the kinetic energy barrier in the reaction process by setting a suitable collective variable (CV, ξ), which changes from state 1 to state 2 at a certain transformation rate $\dot{\xi}$. The work performed throughout the entire process from state 1 to state 2 can be calculated using the following formula:

$$W_{state1 \rightarrow state2} = \int_{\xi(state1)}^{\xi(state2)} \left(\frac{\partial V(q)}{\partial \xi} \right) \cdot \dot{\xi} dt$$

Where $V(q)$ represents the free energy, and $\frac{\partial V(q)}{\partial \xi}$ is calculated using the SHAKE

algorithm. When approaching the infinitesimal limit $\dot{\xi}$, the work $W_{state1 \rightarrow state2}$ required from state 1 to state 2 corresponds to the difference in free energy. In the SG

sampling method, $\partial\xi$ is selected to 0.0005Å, and the final reaction's free energy barrier can be obtained by aggregating the free energy distribution diagram.

References

1. Buttignol, F. *et al.* Iron-catalysed cooperative redox mechanism for the simultaneous conversion of nitrous oxide and nitric oxide. *Nat. Catal.* **7**, 1305–1315 (2024).
2. Ghosh, P. *et al.* Get to Know NO. *Nat. Chem.* **16**, 1382 (2024).
3. Hwang, J. *et al.* Regulating oxygen activity of perovskites to promote NO_x oxidation and reduction kinetics. *Nat. Catal.* **4**, 663–673 (2021).
4. Anenberg, S. *et al.* Impacts and mitigation of excess diesel-related NO_x emissions in 11 major vehicle markets. *Nature* **545**, 467–471 (2017).
5. Han, L. *et al.* Selective catalytic reduction of NO_x with NH₃ by using novel catalysts: state of the art and future prospects. *Chem. Rev.* **119**, 10916–10976 (2019).
6. He, G. *et al.* Polymeric vanadyl species determine the low-temperature activity of V-based catalysts for the SCR of NO_x with NH₃. *Sci. Adv.* **4**, eaau4637 (2018).
7. Gevers, L. *et al.* Unraveling the structure and role of Mn and Ce for NO_x reduction in application-relevant catalysts. *Nat. Commun.* **13**, 2960 (2022).
8. Inomata, Y. *et al.* Bulk tungsten-substituted vanadium oxide for low-temperature NO_x removal in the presence of water. *Nat Commun.* **12**, 557 (2021).

9. Marberger, A. et al. VO_x surface coverage optimization of V₂O₅/WO₃-TiO₂ SCR catalysts by variation of the V loading and by aging. *Catalysts* **5**, 1704–1720 (2015).
10. Kwak, J. H. et al. Excellent activity and selectivity of Cu-SSZ-13 in the selective catalytic reduction of NO_x with NH₃. *J. Catal.* **275**, 187–190 (2010).
11. Shao, J. et al. Electrochemical synthesis of ammonia from nitric oxide using a copper–tin alloy catalyst. *Nat. Energy* **8**, 1273–1283 (2023).
12. Liang, J. et al. Amorphous boron carbide on titanium dioxide nanobelt arrays for high-efficiency electrocatalytic NO reduction to NH₃. *Angew. Chem. Int. Ed.* **61**, e202202087 (2022).
13. Zhang, L. et al. High-performance electrochemical NO reduction into NH₃ by MoS₂ nanosheet. *Angew. Chem. Int. Ed.* **60**, 25263–25268 (2021).
14. John, J. et al. The why and how of NO_x electroreduction to ammonia. *Nat. Catal.* **6**, 1125–1130 (2023).
15. Salmon, N. et al. Offshore green ammonia synthesis. *Nat. Synth.* **2**, 604–611 (2023).
16. Wang, D. et al. Hexagonal cobalt nanosheets for high-performance electrocatalytic NO reduction to NH₃. *J. Am. Chem. Soc.* **145**, 6899–6904 (2023).
17. Wu, Z. et al. Cu@Co with dilatation strain for high-performance electrocatalytic reduction of low-concentration nitric oxide. *Adv. Mater.* **36**, 2309470 (2024).
18. Li, Y. et al. Electrocatalytic reduction of low-concentration nitric oxide into ammonia over Ru nanosheets. *ACS Energy Lett.* **7**, 1187–1194 (2022).

19. Guo, X. et al. Aqueous electroreduction of nitric oxide to ammonia at low concentration via vacancy engineered FeOCl. *Angew. Chem. Int. Ed.* **63**, e202318792 (2024).
20. Guo, X. et al. Enhancing low-concentration electroreduction of NO to NH₃ via potential-controlled active site-intermediate interactions. *Angew. Chem. Int. Ed.* **64**, e202420346 (2025).
21. Wang, D. et al. Ru-incorporation-induced phase transition in Co nanoparticles for low-concentration nitric oxide electroreduction to ammonia at low potential. *Adv. Mater.* **36**, 2408580 (2024).
22. Wang, D. et al. Oxygen-bridged copper-iron atomic pair as dual-metal active sites for boosting electrocatalytic NO reduction. *Adv. Mater.* **35**, 2304646 (2023).
23. Liang, J. et al. Coupling denitrification and ammonia synthesis via selective electrochemical reduction of nitric oxide over Fe₂O₃ nanorods. *J. Mater. Chem. A* **10**, 6454 (2022).
24. Wu, T. et al. Greatly improving electrochemical N₂ reduction over TiO₂ nanoparticles by iron doping. *Angew. Chem. Int. Ed.* **58**, 18449-18453 (2019).
25. Kang, W. et al. Structural evidence for a dynamic metallocofactor during N₂ reduction by Mo-nitrogenase. *Science* **368**, 1381 (2020).
26. Wang, C. et al. Advanced noble-metal/transition-metal/metal-free electrocatalysts for hydrogen evolution reaction in water-electrolysis for hydrogen production. *Coordin. Chem. Rev.* **514**, 215899 (2024).

27. Li, J. et al. Identification of durable and non-durable FeN_x sites in Fe–N–C materials for proton exchange membrane fuel cells. *Nat. Catal.* **4**, 10–19 (2021).
28. Spivey, T. D. et al. Selective Interactions between free-atom-like d-States in single-atom alloy catalysts and near-frontier molecular orbitals. *J. Am. Chem. Soc.* **143**, 11897–11902 (2021).
29. Wan, X. et al. Iron atom–cluster interactions increase activity and improve durability in Fe–N–C fuel cells. *Nat. Commun.* **13**, 2963 (2022).
30. Xian, J. et al. Electrocatalytic synthesis of essential amino acids from nitric oxide using atomically dispersed Fe on N-doped carbon. *Angew. Chem. Int. Ed.* **62**, e202304007 (2023).
31. Nie, N. et al. Superfast synthesis of densely packed and ultrafine Pt–lanthanide@KB via solvent-free microwave as efficient hydrogen evolution electrocatalysts. *Small* **17**, 2102879 (2021).
32. Gao, X. et al. Mechanism of particle-mediated inhibition of demetalation for single-atom catalytic sites in acidic electrochemical environments. *J. Am. Chem. Soc.* **145**, 15528–15537 (2023).
33. Kim, D. et al. Selective electrochemical reduction of nitric oxide to hydroxylamine by atomically dispersed iron catalyst. *Nat. Commun.* **12**, 1856 (2021).
34. Yao, Y. et al. Electrochemical nitrogen reduction reaction on ruthenium. *ACS Energy Lett.* **4**, 1336–1341 (2019).

35. Fang, J. et al. Ampere-level current density ammonia electrochemical synthesis using CuCo nanosheets simulating nitrite reductase bifunctional nature. *Nat. Commun.* **13**, 7899 (2022).
36. Li, J. et al. Efficient ammonia electrosynthesis from nitrate on strained ruthenium nanoclusters. *J. Am. Chem. Soc.* **142**, 7036–7046 (2020).
37. Wang, Y. et al. Phase-regulated active hydrogen behavior on molybdenum disulfide for electrochemical nitrate-to-ammonia conversion. *Angew. Chem. Int. Ed.* **63**, e202315109 (2024).
38. Zhou, J. et al. Linear adsorption enables NO selective electroreduction to hydroxylamine on single Co sites. *Angew. Chem. Int. Ed.* **62**, e202305184 (2023).
39. Han, S. et al. Ultralow overpotential nitrate reduction to ammonia via a three-step relay mechanism. *Nat. Catal.* **6**, 402–414 (2023).
40. Chen, K. et al. Self-tandem electrocatalytic NO reduction to NH₃ on a W single-atom catalyst. *Nano Lett.* **23**, 1735–1742 (2023).
41. Cheon, S. et al. Electro-synthesis of ammonia from dilute nitric oxide on a gas diffusion electrode. *ACS Energy Lett.* **7**, 958–965 (2022).
42. Li, M. et al. A pair-electrosynthesis for formate at ultra-low voltage via coupling of CO₂ reduction and formaldehyde oxidation. *Nano-Micro Lett.* **14**, 211 (2022).
43. Zhu, D. et al. Photo-illuminated diamond as a solid-state source of solvated electrons in water for nitrogen reduction. *Nat. Mater.* **12**, 836–841 (2013).
44. Mortensen, J. J. et al. Real-space grid implementation of the projector augmented wave method. *Phys. Rev. B* **71**, 035109 (2005).

45. Enkovaara, J. et al. Electronic structure calculations with GPAW: a real-space implementation of the projector augmented-wave method. *J. Phys. Condens. Matter* **22**, 253202 (2010).
46. Held, A. et al. Simplified continuum solvent model with a smooth cavity based on volumetric Data. *J. Chem. Phys.* **141**, 174108 (2014).
47. Peterson, A. A. Global optimization of adsorbate-surface structures while preserving molecular identity, *Top. Catal.* **57**, 40-53 (2014).
48. Larsen, A. H. et al. The atomic simulation environment—a Python library for working with atoms, *J. Phys. Condens. Matter* **29**, 273002 (2017).
49. Woo, T. K. et al. A combined car–Parrinello QM/MM implementation for Ab initio molecular dynamics simulations of extended systems: application to transition metal catalysis. *J. Phys. Chem. B* **101**, 7877–7880 (1997).
50. Jarzynski, C. Nonequilibrium equality for free energy differences. *Phys. Rev. Lett.* **78**, 2690–2693 (1997).

Acknowledgements

This work was supported by National Natural Science Foundation of China (Nos. 22072015, 21927811, and 52202214), Natural Science Foundation of Sichuan Province (No. 2023NSFSC0954), China National Postdoctoral Program for Innovative Talents (No. BX2021053), and China Postdoctoral Science Foundation (No. 2021M700680). The authors thank BL11B beamline of the Shanghai Synchrotron Radiation Facility (SSRF) for providing the XAFS beamtime. The numerical calculations in this paper have been done on Computing Center in Xi'an.

Contributions

T.W. and X.G. conceived the idea, wrote the original draft, and collected and analyzed the data. X.G. and T.W. performed the DFT calculations and experiments. C.M. provided the HAADF-STEM characterization. M.L. supervised this project. All authors contributed and reviewed the manuscript.

Competing interests

The authors declare no competing financial interests.

Additional information

Correspondence and requests for materials should be addressed to M.L.

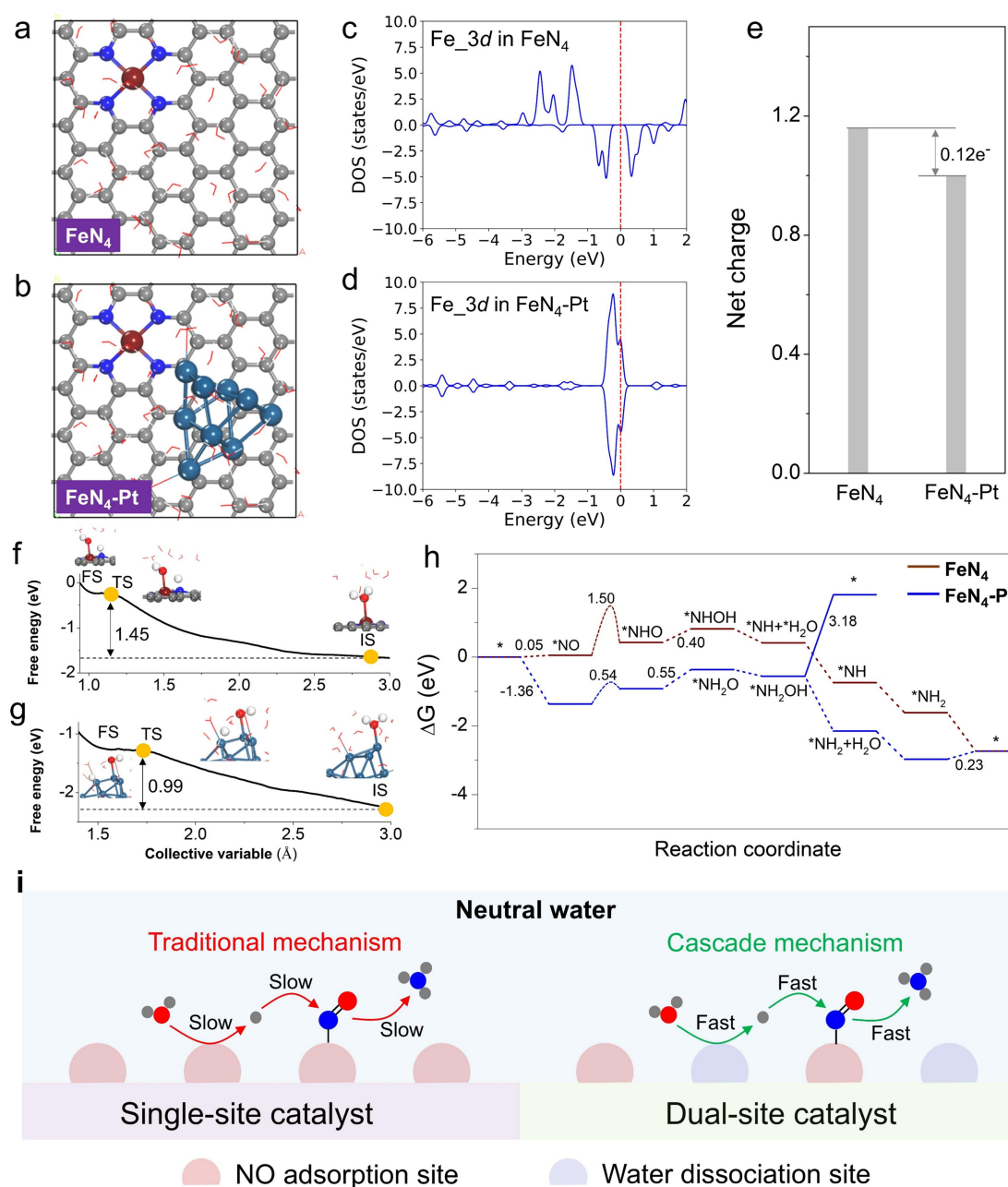


Fig. 1 | Theoretical calculations. Atom configurations of (a) FeN₄ and (b) FeN₄-Pt. Corresponding DOS plots of Fe atom in (c) FeN₄ and (d) FeN₄-Pt. (e) Bader charge analysis of Fe atom in FeN₄ and FeN₄-Pt, respectively. (f) The reaction free energies of NORR pathways on FeN₄ and FeN₄-Pt. The free energy of water dissociation on (g) FeN₄ and (h) FeN₄-Pt. (i) Comparison between traditional and cascade mechanisms.

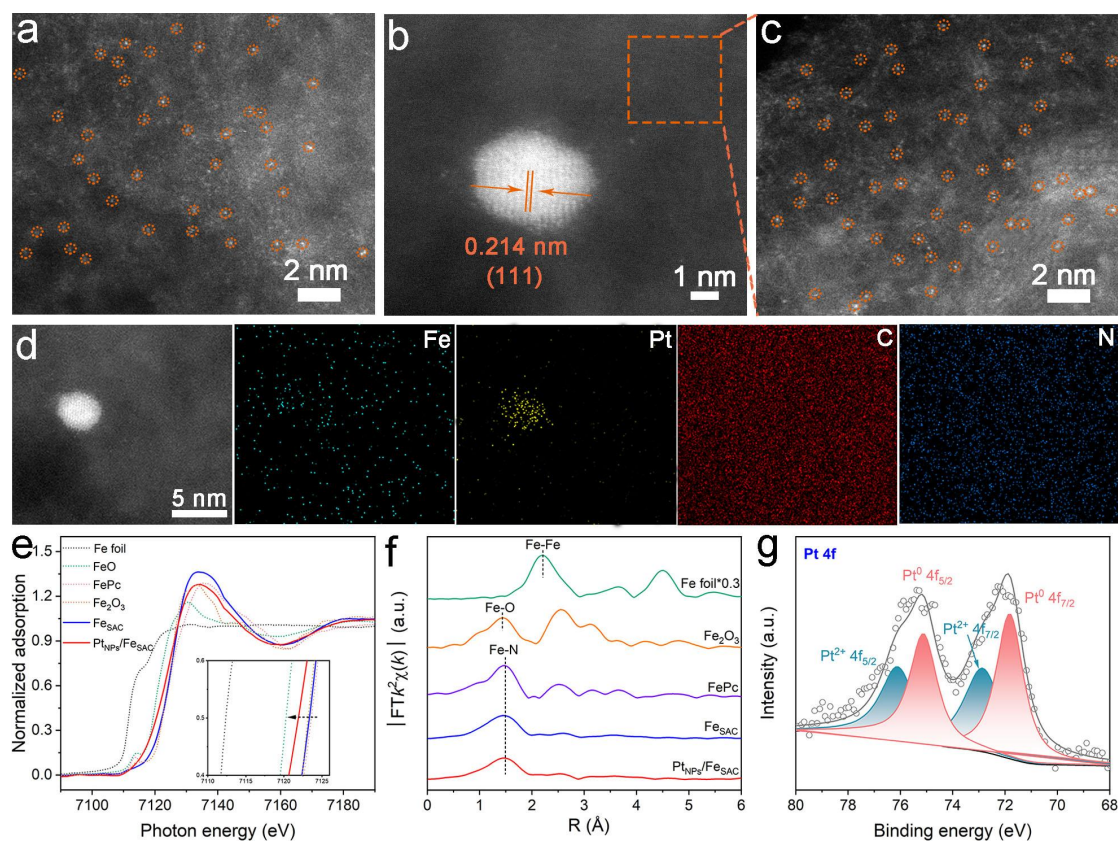


Fig. 2 | Structural characterizations of catalysts. HAADF-STEM images of (a) FeSAC and (b, c) PtNPs/FeSAC. (d) EDX mapping images of PtNPs/FeSAC. (e) Fe K-edge XANES spectra of Fe foil, FePc, Fe₂O₃, FeSAC and PtNPs/FeSAC. (f) FT-EXAFS spectra at Fe K-edge. (g) XPS spectrum of PtNPs/FeSAC in Pt 4f region.

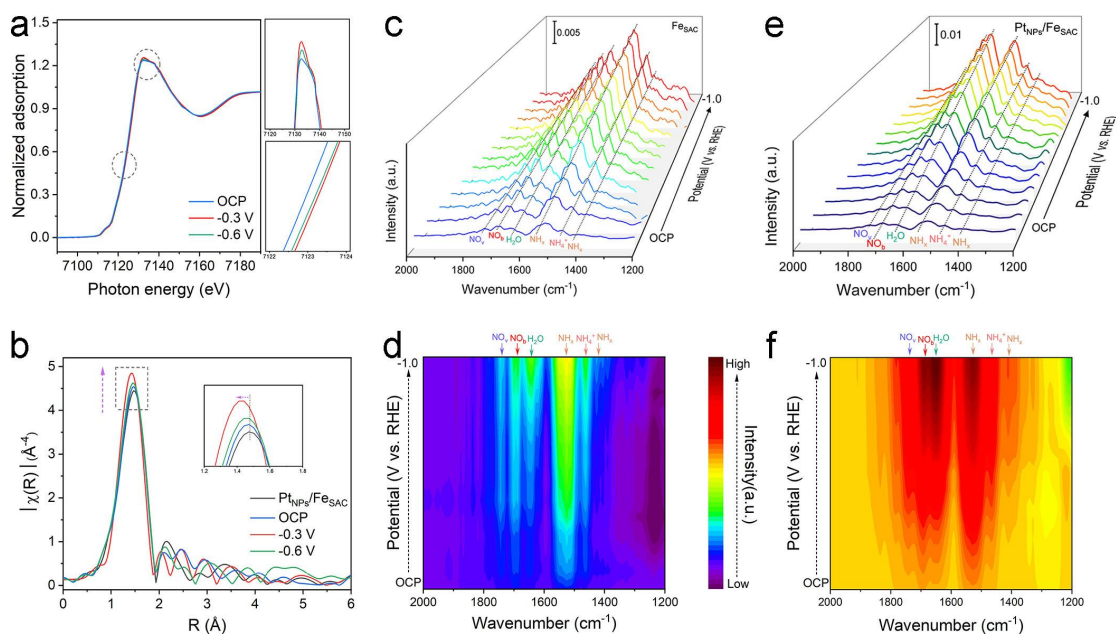


Fig. 3 | *In situ* XAS and ATR-IR spectra of NORR. (a) *In situ* Fe K-edge XANES spectra of Pt_{NPs}/Fe_{SAC} at different potentials. (Inset) Magnified white-line peak and pre-edge XANES region. (b) Corresponding FT-EXAFS spectra at Fe K-edge. Potential-dependent *in situ* ATR-IR spectra of (c) Fe_{SAC} and (e) Pt_{NPs}/Fe_{SAC}. Corresponding 2D ATR-IR contour map of (d) Fe_{SAC} and (f) Pt_{NPs}/Fe_{SAC}.

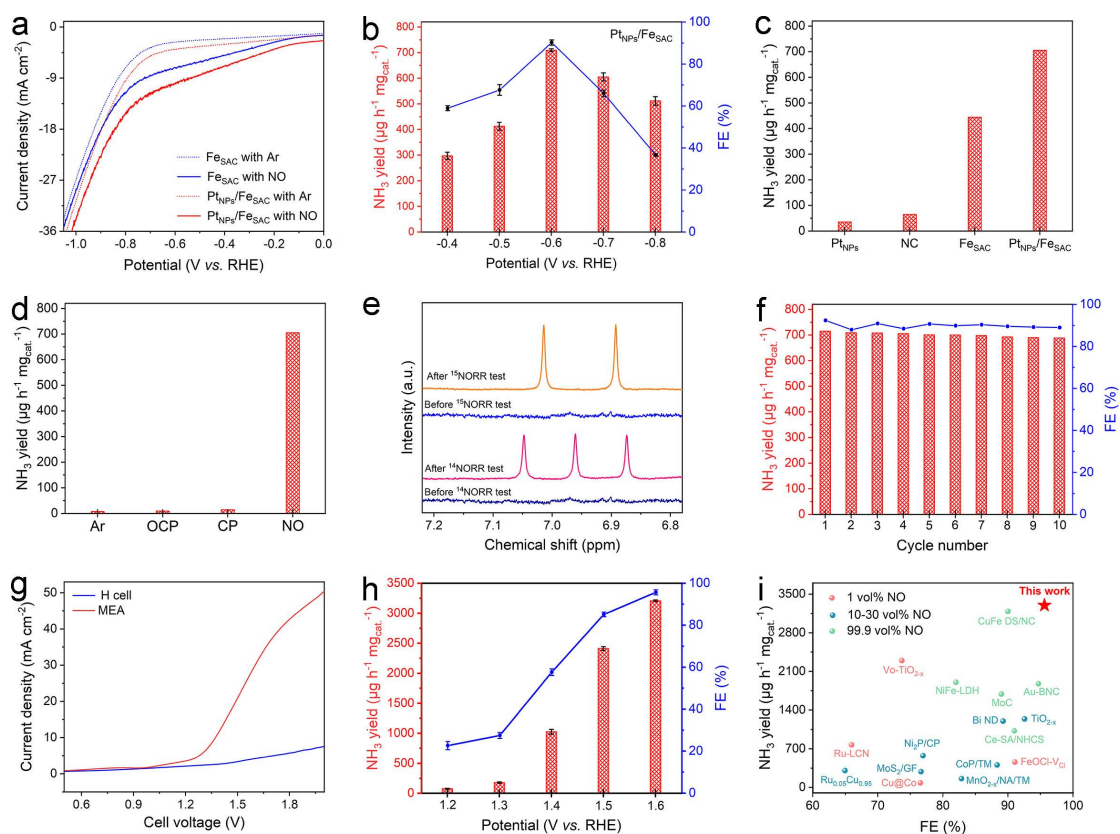


Fig. 4 | Electrochemical NORR performance. (a) LSV curves of FeSAC and PtNPs/FeSAC in Ar- and 1 vol% NO-saturated 0.5 M K₂SO₄. (b) NH₃ yield and FE with 1 vol% NO over PtNPs/FeSAC at each given potential. (c) The NH₃ yield of PtNPs, NC, FeSAC and PtNPs/FeSAC. (d) NH₃ yield of PtNPs/FeSAC under different conditions. (e) ¹H NMR spectra of the electrolyte fed by ¹⁵NO and ¹⁴NO for NORR over the PtNPs/FeSAC at -0.6 V. (f) NORR cycling stability test over the PtNPs/FeSAC at -0.6 V. (g) LSV curves of PtNPs/FeSAC test in MEA electrolyzer and H cell. (h) Corresponding NH₃ yield and FE of PtNPs/FeSAC. (i) Comparison of NORR performance with other electrocatalysts.